



## Magneto-ionic suppression of magnetic vortices

Yu Chen, Aliona Nicolenco, Pau Molet, Agustin Mihi, Eva Pellicer & Jordi Sort

To cite this article: Yu Chen, Aliona Nicolenco, Pau Molet, Agustin Mihi, Eva Pellicer & Jordi Sort (2021) Magneto-ionic suppression of magnetic vortices, Science and Technology of Advanced Materials, 22:1, 972-984, DOI: [10.1080/14686996.2021.1988830](https://doi.org/10.1080/14686996.2021.1988830)

To link to this article: <https://doi.org/10.1080/14686996.2021.1988830>



© 2021 The Author(s). Published by National Institute for Materials Science in partnership with Taylor & Francis Group.



[View supplementary material](#)



Published online: 04 Nov 2021.



[Submit your article to this journal](#)



Article views: 1767



[View related articles](#)



[View Crossmark data](#)

## Magneto-ionic suppression of magnetic vortices

Yu Chen <sup>a</sup>, Aliona Nicolenco <sup>a</sup>, Pau Molet <sup>b</sup>, Agustin Mihi <sup>b</sup>, Eva Pellicer <sup>a</sup> and Jordi Sort <sup>a,c</sup>

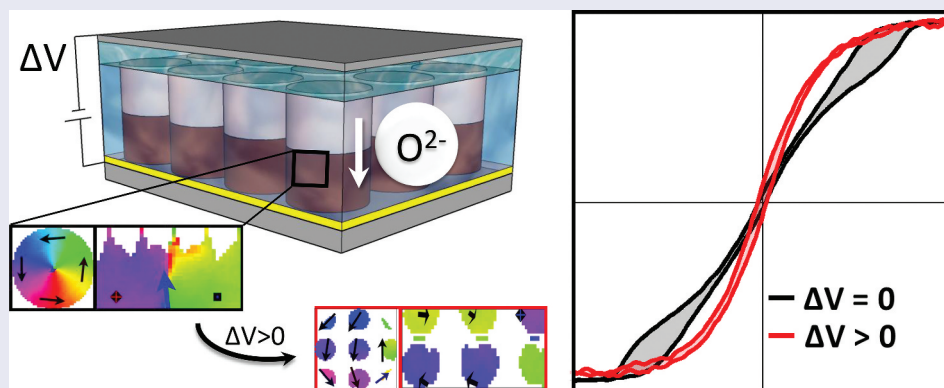
<sup>a</sup>Departament de Física, Universitat Autònoma de Barcelona, Bellaterra, 08193, Spain;

<sup>b</sup>Institute of Materials Science of Barcelona, Bellaterra, 08193, Spain;

<sup>c</sup>Institució Catalana de Recerca i Estudis Avançats, Pg. Lluís Companys 23, Barcelona, 08010, Spain

### ABSTRACT

Magneto-ionics refers to the non-volatile control of the magnetic properties of materials by voltage-driven ion migration. This phenomenon constitutes one of the most important magneto-electric mechanisms and, so far, it has been employed to modify the magnetic easy axis of thin films, their coercivity or their net magnetization. Herein, a novel magneto-ionic effect is demonstrated: the transition from vortex to coherent rotation states, caused by voltage-induced ion motion, in arrays of patterned nanopillars. Electrolyte-gated Co/GdO<sub>x</sub> bilayered nanopillars are chosen as a model system. Electron microscopy observations reveal that, upon voltage application, oxygen ions diffuse from GdO<sub>x</sub> to Co, resulting in the development of paramagnetic oxide phases (CoO<sub>x</sub>) along sporadic diffusion channels. This breaks up the initial magnetization configuration of the ferromagnetic pillars (i.e. vortex states) and leads to the formation of small ferromagnetic nanoclusters, embedded in the CoO<sub>x</sub> matrix, which behave as single-domain nanoparticles. As a result, a decrease in the net magnetic moment is observed, together with a drastic change in the shape of the hysteresis loop. Micromagnetic simulations are used to interpret these findings. These results pave the way towards a new potential application of magneto-electricity: the magneto-ionic control of magnetic vortex states.



### ARTICLE HISTORY

Received 19 July 2021

Revised 28 September 2021

Accepted 29 September 2021

### KEYWORDS

Magnetolectric; magneto-ionics; vortex; voltage control of magnetism

### CLASSIFICATIONS

40 Optical; magnetic and electronic device materials; 102 Porous / Nanoporous / Nanostructured materials < 100 Materials; 106 Metallic materials < 100 Materials; 203 Magnetics / Spintronics / Superconductors < 200 Applications; 212 Surface and interfaces < 200 Applications; 503 TEM, STEM, SEM < 500 Characterization


## 1. Introduction

Magnetic vortex is one of fundamental magnetization states that occurs in micro-/nano sized ferromagnetic structures, e.g. disks, ellipses or nanowires, and so on, due to geometrical spin confinement [1–4]. This state is highly appealing for non-volatile magnetic memories and spintronic devices since the magnetic information can be stored by encoding both (i) the vortex chirality, i.e. the direction of in-plane magnetization rotation (clockwise or counter-clockwise), and (ii) the polarity, i.e. the out-of-plane magnetization of the nanoscale vortex core (up or down) [5]. Hence, each magnetic vortex can store four bits of information. Nonetheless, the applications of magnetic vortices

extend far beyond memory applications, and also include oscillators for effective microwave generation [6], energy storage [7], or biomedical applications (theragnostics) where the magnetic vortices are capable of damaging the membrane of cancer cells or promote drug delivery [8,9]. In turn, single-domain magnetic nanoparticles have found applications in, e.g., high-density recording media, magnetic biosensing, magnetic imaging, or hyperthermia therapy, among others [10].

Traditionally, the magnetic behavior of nanostructures is controlled during sample preparation by varying the aspect ratio of the motifs [1,11,12]. Namely, by increasing the thickness of a circular nanostructure

**CONTACT** Aliona Nicolenco  [Aliona.Nicolenco@uab.cat](mailto:Aliona.Nicolenco@uab.cat); Jordi Sort  [Jordi.Sort@uab.cat](mailto:Jordi.Sort@uab.cat)  Science faculty, Building Cc, Departament de Física, Universitat Autònoma, Bellaterra 08193, Spain

 Supplemental data for this article can be accessed [here](#).

© 2021 The Author(s). Published by National Institute for Materials Science in partnership with Taylor & Francis Group.

This is an Open Access article distributed under the terms of the Creative Commons Attribution License (<http://creativecommons.org/licenses/by/4.0/>), which permits unrestricted use, distribution, and reproduction in any medium, provided the original work is properly cited.

while keeping a fixed diameter, several ferromagnetic states can be generated, such as in-plane single domain, vortex, flower, or out-of-plane single-domain states, respectively. The occurrence of magnetic vortices, particularly in soft magnetic materials (e.g. Ni, NiFe, CoFe, FeGa, Co, etc.), can be predicted from well-established phase diagrams. Thus, arrays of patterned dots with desired magnetic states can be prepared on-demand according to these data [1,11,13–15]. However, the magnetic properties of the as-prepared materials cannot be straightforwardly modified after sample preparation. This limits the versatility and potential functional applications of these nanostructures. To overcome this limitation, significant research effort has been put forward over the years to tune the properties of magnetic vortices by external means, such as spin-torque effects using spin-polarized currents [16,17], laser pulse excitation [18,19], mechanical actuation (e.g. unidirectional compression) [20] or exchange coupling with an adjacent antiferromagnetic layer (after suitable heat treatments and field cooling procedures) [2,21,22]. Nonetheless, these methods are energetically costly and sometimes only induce volatile changes in the vortex properties.

In parallel, during the last few years, a number of investigations have demonstrated the possibility to tailor the magnetic properties of materials at the ‘post-synthesis’ stage using electric fields through the so-called magnetoelectric (ME) effect. This is very appealing because the use of voltage (instead of electrical currents) minimizes Joule heating effects and it can thus be considered as a highly energy-efficient actuation protocol [23]. Voltage has been shown to induce changes in the coercivity [24], net magnetization [25], remanence [26], exchange bias [27], Curie temperature [28] and magnetoresistance [29,30], of the investigated materials. Several ME mechanisms have been identified: intrinsic ME coupling in single-phase multiferroics, electric surface charging in ultra-thin films, magneto-ionics (voltage-driven ion migration), and strain-mediated effects in piezoelectric/magnetostrictive composites [31–33]. ME approaches have rapidly gained significant interest in the design of ultra low-heat-dissipating memories, logic devices, neuromorphic computing or lab-on-chip platforms, among others.

Up to date, ME effects have allowed experimental realization of several types of ‘magnetic switches’: (i) OFF/ON switching of magnetization, when the starting material is non-magnetic but a magnetic phase is generated upon electric field application (and vice versa), via magneto-ionics, strain, or surface charging mechanisms [25,34–36]; (ii) switching between superparamagnetic and single-domain states in nanocrystals, either magneto-ionically or via strain [37,38]; (iii) magneto-resistive switching between low and high

resistance states, also magneto-ionically or by strain [39,40], and (iv) anisotropy easy axis magneto-ionic switching, from in-plane to out-of-plane directions [41,42]. So far, magneto-ionic switching from vortex to single-domain states has not been demonstrated.

ME manipulation of magnetic vortex properties has been achieved using strain transfer from an underlying ferroelectric material. Micromagnetic simulations first predicted the possibility to switch between the magnetic vortex and polar states in FeGa nanodots grown onto a ferroelectric PZT substrate [15]. Later on, experimental works showed annihilation of magnetic vortices in Ni disks via uniaxial compressive strain transferred from PMN-PT [43] or BaTiO<sub>3</sub> [44]. Electric-field-assisted switching of magnetic vortex chirality was also shown in Co/PMN-PT [45]. While these results are very appealing for voltage-control of vortex states, the complicated behavior of the ferroelectric domains of these substrates (including ferroelectric relaxor phenomena [46] and presence of surface skin layers [47]) poses some challenges to obtain uniform magnetization reversal modes in all disks comprised patterned arrays. This adds to other important issues of strain-mediated ME systems, such as clamping effects, mechanical fatigue, high fabrication costs (in the case of PMN-PT) or need of relatively large applied voltages (e.g. 400 V) [43].

Among all converse ME effects, magneto-ionics is gaining attention because voltage-driven ion transport between the magnetic material of interest and an ion source/sink allows for a stringent non-volatile control of interfacial magnetism to an unprecedented extent [25,48,49]. Upon electrolyte gating, the ions may form diffusion channels or even uniform migration fronts (eventually developing new interfaces within the actuated films), resulting in unique magnetic characteristics (in e.g. oxides or nitrides) [25,48]. Magneto-ionic effects can involve the transport of various types of ion species, such as alkali metal cations (Li<sup>+</sup>, Na<sup>+</sup> and K<sup>+</sup>) [50–52], H<sup>+</sup> [49,53], F<sup>−</sup> [54], N<sup>3−</sup> [48], and O<sup>2−</sup>. The latter remains the most studied up to date. Interesting effects have been reported both in transition-metal oxide single layers, where the oxygen ions are already present in the original material structure [25,55,56], and in ME heterostructures where the oxygen ions are supplied to the magnetic material of interest from an adjacent high ionic mobility ion reservoirs, such as Gd<sub>2</sub>O<sub>3</sub> [34,49,57–60], HfO<sub>2</sub> [61–63], or Al<sub>2</sub>O<sub>3</sub> [41,64,65] layers.

In this work, we investigate a new room-temperature magneto-ionic effect that is induced at the nanoscale: the transition from ‘magnetic vortex state’ to ‘coherent rotation’ in electrolyte-gated Co/GdO<sub>x</sub> bilayered nanopillars. Upon voltage application, oxygen diffuses from the GdO<sub>x</sub> solid ionic conductor towards metallic Co, forming a non-magnetic CoO<sub>x</sub> matrix with embedded Co nanoclusters which

enable vortex suppression. The experimental results are interpreted with the aid of micromagnetic simulations to model magnetization behavior in the pristine pillars (at 0 V) and after voltage actuation. The challenges and future research directions for further optimization and control of this newly observed magneto-ionic effect are described.

## 2. Experimental section

Cobalt nanopillars were grown by electrodeposition of the metal on Au (80 nm)/Ti (20 nm)/Si substrates coated with a patterned resist film (Figure 1(a)) featuring a square array of cylindrical holes of 200 nm in diameter, 400 nm pitch and 280 nm in height. The patterns were obtained by nanoimprinting 280–300 nm thick film of SU8 2000.5 (Microchem, Germany) photoresist with pre-patterned polydimethylsiloxane (PDMS) molds [66]. This technique has been proven capable of producing extended nanostructured areas with high fidelity, rapidity, cleanroom-free and at a low cost [67,68]. After the pattern is imprinted on the resist, the Au seed-layer on the substrate was exposed on the patterned areas by performing reactive ion etching using O<sub>2</sub> plasma.

The resulting pattern was used as a template for electrodeposition of Co pillars. Electrodeposition was performed in a three-electrode single compartment cell connected to a PGSTAT302N Autolab potentiostat/galvanostat (Metrohm-Autolab, The Netherlands). A double junction Ag/AgCl reference electrode (Metrohm AG, Switzerland) was used with 3 M KCl inner solution and 1 M Na<sub>2</sub>SO<sub>4</sub> outer solution, and a Pt wire served as a counter electrode.

Electrodeposition was done from an electrolytic bath with the following composition: 0.2 M CoSO<sub>4</sub>·7H<sub>2</sub>O, 0.65 M H<sub>3</sub>BO<sub>3</sub>, 0.25 M Na<sub>3</sub>C<sub>6</sub>H<sub>5</sub>O<sub>7</sub> and 0.04 M C<sub>6</sub>H<sub>8</sub>O<sub>7</sub> [69]. The pH was left at its unadjusted value (4.6). Co nanopillars were grown potentiostatically at –1.00 V under stagnant conditions at room temperature. From the representative current–time curve shown in Supporting Figure S1 it can be concluded that Co grows inside the template for ~100 s and then overgrows, tending to form a continuous layer for longer deposition times. A preliminary magnetic characterization study revealed that magnetic vortex behavior (i.e. constricted hysteresis loops) was observed in Co pillars produced after depositing for 20–60 seconds, which corresponds to 60–120 nm thickness. This is in agreement with the vortex vs. coherent rotation experimental phase diagram for Co disks/pillars reported in the literature, which predicts vortex state for this range of thicknesses-to-diameter aspect ratios [1,11]. For the magneto-ionic actuation, nanopillars with 80 nm thickness were selected. Note that nanostructures with lower thickness and flat surface are difficult to produce by electrodeposition, due to the complex nucleation and growth mechanisms which result in a rough topography and local thickness variation. Next, a 40 nm ± 5 nm layer of GdO<sub>x</sub> was deposited on top of the template partially filled with Co using magnetron sputtering (Figure 1(a)) at room temperature with a base pressure around 10<sup>–8</sup> Torr. The flows of high-purity Ar and O<sub>2</sub> were 17 sccm and 10 sccm, respectively, with a total pressure of 3 × 10<sup>–3</sup> mbar. The distance between the target and the substrate was around 8 cm, and the deposition rate was about 0.36 Å s<sup>–1</sup>. The photoresist template was not

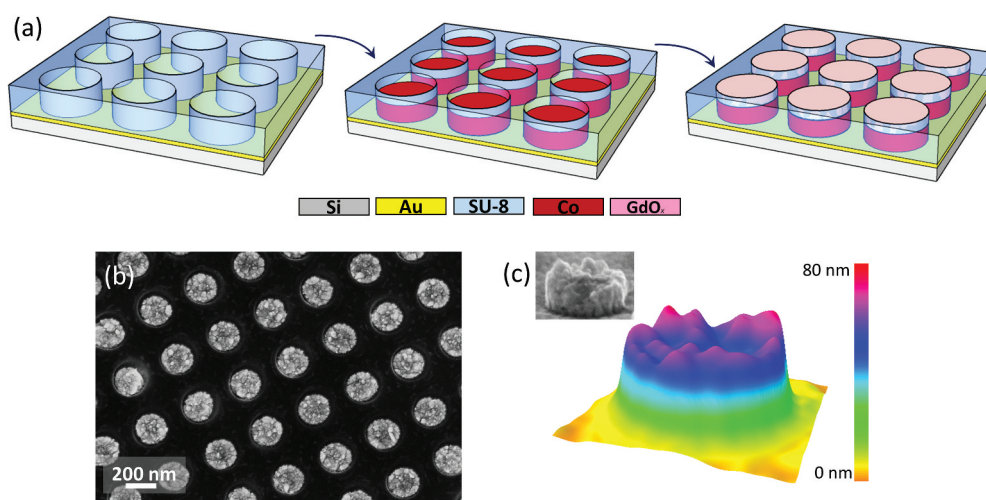


**Figure 1.** (a) Schematics of the synthesis procedure to grow bilayered nanopillars, wherein Co is first electrodeposited on a nanoimprinted substrate and GdO<sub>x</sub> is subsequently sputtered on top (note that for sake of clarity the GdO<sub>x</sub> that grew on top of the SU-8 resist is not shown). (b) Representative SEM image of an array of electrodeposited Co nanopillars embedded in SU-8 template (before sputtering GdO<sub>x</sub>). (c) Reconstructed 3D profile of an individual as-deposited Co nanopillar (without GdO<sub>x</sub>) obtained after processing the SEM micrograph with ImageJ software. The inset in panel (c) shows a FE-SEM image of a single as-grown Co pillar.

removed at any stage of sample preparation in order not to distort the Co/GdO<sub>x</sub> bilayer structure of the pillars (i.e. to maintain one horizontal interface).

Surface morphology and composition of the samples were characterized on a Zeiss Merlin (Zeiss, Germany) field emission scanning electron microscope (FE-SEM) equipped with an energy-dispersive X-ray (EDX) detector, and the 'Image J' software [70] was used to reconstruct the topography of the as-deposited nanopillars. High-angle annular dark-field scanning transmission electron microscopy (HAADF-STEM) and electron energy loss spectroscopy (EELS) were performed using a JEOL JEM2010F microscope (Jeol, Japan) equipped with a field emission gun, operated at 200 kV and coupled to a Gatan GIF spectrometer.

A MicroSense (LOT-QuantumDesign, United States) Vibrating Sample Magnetometer (VSM) was used to perform magnetoelectric measurements. The voltage was applied in-situ using a home-made two-electrode electrochemical cell connected to the Agilent B2902A (Agilent Technologies, United States) power supply and attached to a VSM sample holder, as described in detail in our previous works [71]. The sample with the Co/GdO<sub>x</sub> nanopillars of approximately 0.25 cm<sup>2</sup> size acted as a working electrode and the contact was made to the underlying Au seed layer in a capacitor-like configuration [72]. A Pt wire was used as counter electrode. The electrodes were placed in a small Eppendorf tube (1 ml) filled with an anhydrous electrolyte. The electrolyte solution was propylene carbonate treated with metallic sodium to remove any traces of water. The sodium treatment left a small amount of Na<sup>+</sup> and OH<sup>-</sup> ions, and no other salts were added. The use of a liquid electrolyte is advantageous because it allows the generation of ultra-high electric fields (of the order of hundreds of MV cm<sup>-1</sup>), without electric pinholes or defects in a thin layer of GdO<sub>x</sub>. All magnetic measurements were taken at room temperature in an in-plane configuration, while the voltage was applied out-of-plane. Prior to measuring each hysteresis loop a specific negative voltage was applied for 30 min following this sequence: 0–60 V with a step of 10 V, and 80–280 V with a step of 20 V. In all cases, voltage was maintained during the measurement (each hysteresis loop takes 30 min to be completed), which resulted in a total voltage application time of 1 h at each specific condition. A waiting time of 15 min was allowed between each voltage switch.

Micromagnetic modeling was performed using the micromagnetic simulator Object Oriented MicroMagnetic Framework (OOMMF) [73]. The following parameters were used for hexagonal close-packed (hcp)-Co: exchange constant  $A = 30 \text{ pJ m}^{-1}$ , anisotropy  $K_1 = 430 \text{ kJ m}^{-3}$  chosen to be along random directions among cells (polycrystalline Co) and saturation magnetization  $M_s = 1100 \text{ emu cm}^{-3}$  (somewhat

lower than for bulk Co, as it has been reported for electrodeposited Co due to the presence of impurities) [1,74]. The cell size was set to 5 nm. To reproduce the nanopillars with upper rough surface, the geometry was defined as a cylinder with disordered arrays of little cones with different sizes and pitch. The energy minimization evolver was adopted to obtain the magnetization configuration at different values of applied magnetic field.

### 3. Results and discussion

Magnetic nanopillars comprising electrodeposited Co and sputtered GdO<sub>x</sub> layers were prepared onto metalized Si substrates covered with a nanoimprinted resist, as schematically illustrated in Figure 1(a). Figure 1(b) shows a representative top-view SEM micrograph of the as-deposited Co pillars inside the template. The diameter of the pillars is given by the size of the pores and is around 200 nm. The pillars exhibit some roughness (Figure 1(c)) provided by the polycrystalline grain growth during electrodeposition. It is worth mentioning that the polymeric template was not removed at any stage of the experiment. The SU-8 polymer (epoxy-based, negative tone resist) is commonly used in various micro-/nanoelectromechanical systems (MEMS/NEMS) due to its outstanding chemical and thermal resistivity, optical transparency and easy fabrication of high-aspect-ratio features. In addition, it is an electrical insulator (breakdown field  $\sim 10^8 \text{ V m}^{-1}$ ). Thanks to such properties, SU-8 is an ideal material to be fully integrated in electronics, functional MEMS/NEMS devices and lab-on-chip microsystems [75]. Since the Co pillars do not completely fill the pores of the template, sputtering GdO<sub>x</sub> on top of such structures renders an array of bilayered nanopillars with a Co/GdO<sub>x</sub> interface roughly parallel to the substrate.

The magnetic properties of the nanostructures were measured at room temperature using VSM. Figure 2 (a) shows the evolution of the M-H hysteresis loops of the Co/GdO<sub>x</sub> nanopillars as a function of applied positive voltage. In the initial state at 0 V, the shape of the loop indicates magnetization reversal via formation of a vortex state, with its characteristic central constriction, negligible coercivity, small remanent magnetization and clear open lobes at high magnetic fields. Applying positive voltage to the Co/GdO<sub>x</sub> heterostructures significantly alters the shape of the hysteresis loop, as well as the magnetic moment at saturation (Figure 2(b)). The magnetic moment decreases gradually up to 100 V and then remains rather constant even when the voltage is further increased. The decrease of magnetization is in accordance with magneto-ionic phenomena. Upon application of positive voltage, the negatively charged oxygen ions migrate from GdO<sub>x</sub> towards the underlying Co

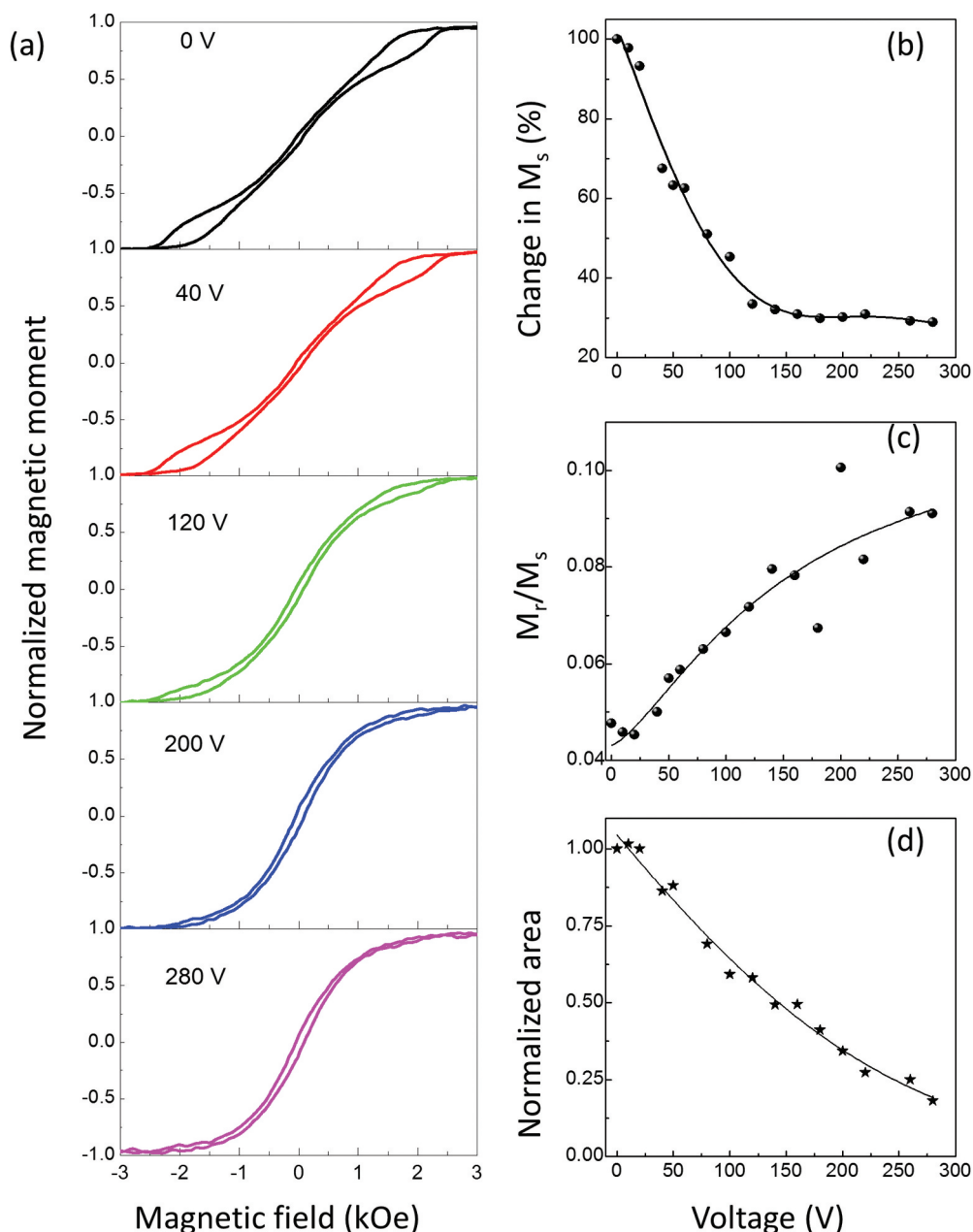


**Figure 2.** Magneto-electric actuation of Co/GdO<sub>x</sub> nanopillars. (a) Representative room-temperature hysteresis loops for gradually increasing values of positive voltage from 0 to 280 V. The loops are normalized to 1 to facilitate comparison of their shapes. Dependence of the (b) change in magnetic moment with respect to 0 V, (c) squareness ratio and (d) normalized area of the loops as a function of the applied voltage where 1 is the area of the loop at 0 V.

layers, driven by the electric field which is induced perpendicularly to the sample surface. This triggers two redox reactions that occur simultaneously: (i) partial Co oxidation by O<sup>2-</sup> to produce CoO<sub>x</sub>; and (ii) partial GdO<sub>x</sub> reduction to metallic Gd. Since both, Gd and CoO<sub>x</sub> phases (both CoO and Co<sub>3</sub>O<sub>4</sub>), are paramagnetic at room temperature, these redox reactions are responsible for the observed decrease in the magnetic moment.

The plateau in Figure 2(b) reached at ~100 V suggests that, most probably, already at this voltage, most of the oxygen ions have been transported towards Co. Hence, further paramagnetic phase fraction does not form. However, the squareness ratio,  $M_r/M_s$  (Figure 2

(c)), and the shape of the hysteresis loop (i.e. the normalized integrated area in Figure 2(d)) continue to evolve even for higher applied positive voltages. Therefore, although the magnetic moment remains rather constant for  $\Delta V > 100$  V, the system does not seem to reach a steady state yet. At  $\Delta V = 120$  V, the hysteresis loop still shows small open lobes characteristic for a magnetic vortex state. Remarkably, neither the nucleation field nor the annihilation field of the vortex varies considerably as a function of applied voltage. However, the irreversible hysteresis loss (i.e. the area enclosed by the hysteresis loop) progressively decreases up to  $\Delta V = 200$  V. Above this voltage, the central constriction and the open lobes of the loops are

no longer observed, suggesting that the vortex state is suppressed. At such high voltages, the loop shape resembles that of polycrystalline cobalt. Since migration of  $O^{2-}$  from  $GdO_x$  is not expected above  $\Delta V = 100$  V, other processes should be responsible for the observed loss of the vortex stability. Indeed, recent magneto-ionic studies in  $CoO_x$  single layers, involving positron annihilation experiments, have revealed a complicated voltage-driven ion transport involving not only  $O^{2-}$  ion migration but also  $Co^{2+}$  cations redistribution while preserving the total net magnetic moment [25,48].

Micromagnetic simulations were performed in order to get a better understanding of the magnetization reversal mechanisms in the voltage-actuated arrays of  $Co/GdO_x$  nanopillars, both at 0 V and after application of positive voltage. Supporting Figure S2(a) compares the experimental loop at 0 V with the simulated hysteresis loop of an individual 'perfect' disk-shaped Co pillar with 200 nm width and 80 nm thickness. The nucleation and annihilation fields obtained from the simulations are in rather good agreement with the experimental data. However, the experimental loop is significantly more tilted than the theoretical prediction. To improve the agreement between experimental and computed loops, the effect of surface roughness was also modeled (by incorporating surface imperfections, such as holes or hills). The results, presented in Supporting Figure S2(b,c) indicate that, indeed, the magnetic behavior of the Co nanopillars is influenced, to some extent, by the surface topological characteristics. Since electrodeposited Co pillars feature noticeable surface inhomogeneities (Figure 1), incorporation of a certain degree of random roughness in the simulations, resembling the topography of electrodeposited Co, is justified. As shown in Supporting Figure S2(d), the occurrence of surface roughness induces variations in the values of nucleation and annihilation fields (i.e. a distribution of the switching fields among pillars). This explains why the nucleation and annihilation events in the experimental loops are not as sharp as in the simulations.

Next, arrays of four cylindrical disks having variable thickness (Supporting Figure S2(e)) and roughness (Figure S2(f)) were also simulated. This allows to better assess the effects of averaging local variations in the nucleation/annihilation fields among dots, as well as possible effects from inter-dot magnetic dipolar interactions. In all cases, for the selected geometries (thickness range between 60 and 90 nm and roughness inhomogeneity with peak-to-valley distances up to 30 nm), vortex-like hysteresis loops were obtained. Interestingly, adding these local inhomogeneities among pillars allows obtaining a better agreement between the simulations and the experimental loops

(which correspond to arrays of hundreds or thousands of Co pillars), i.e. more rounded and sheared hysteresis loops.

Figure 3 illustrates the evolution of the simulated spin configurations corresponding to different values of applied magnetic field for rough Co nanopillars with the geometry depicted in Supporting Figure S2(f) (i.e. magnetization reversal occurring through vortex spin structure). When the magnetic field is decreased from saturation (1), the magnetic vortex nucleates at around 1000 Oe (2–3). This is accompanied by an abrupt decrease in the average dot magnetization. As the magnetic field is further decreased the vortex core progressively displaces towards the center of the disk and at zero magnetic field all the spins follow the circular geometry of the disk (4). When the magnetic field reaches the annihilation field (5), the vortex vanishes completely (6). This occurs at around 2020 Oe. This process stabilizes the single-domain state with negative orientation.

As experimentally demonstrated and shown in Figure 2, voltage actuation significantly changes the magnetic response of the system. Assuming the voltage-driven oxygen transport towards the substrate, a large fraction of metallic Co adjacent to  $GdO_x$  should be converted into paramagnetic  $CoO_x$ , thus resulting in a decrease in the effective thickness of ferromagnetic Co counterpart. Micromagnetic simulations have been employed to model the shape and magnetization reversal behavior of the Co nanopillars after positive (e.g.  $\Delta V = 200$  V) voltage actuation. Assuming that the oxygen moving front is horizontal (parallel to the substrate), one may expect to form a flat  $CoO_x/Co$  interface, where the Co counterpart may retain the initial disk shape and  $CoO_x$  would be on top. Figure 4(a) shows a simulated hysteresis loop of an individual 'perfect' Co disk with a thickness of 25 nm (which roughly corresponds to 1/3 of the initial thickness of the Co pillar, in agreement with the observed decrease in magnetic moment (Figure 2(b))). According to the modeling, this disk-shaped pillar still results in magnetization reversal via vortex spin arrangement, with clear open lobes at high fields and zero net magnetization at remanence. This is actually in agreement with the calculated ground state phase diagram for polycrystalline hcp-Co sub-micrometer dots, wherein the vortex-to-single domain transition occurs at above 20 nm thickness [11]. However, the experimental loop shows a very different behavior, with no constriction in its central part, indicating that reversal is not by vortex-state formation. To see whether a transition from vortex to in-plane single-domain state occurred during the magneto-ionic experiments, we then simulated the magnetization reversal of a thinner (i.e. 15 nm) Co pillar (Figure 4

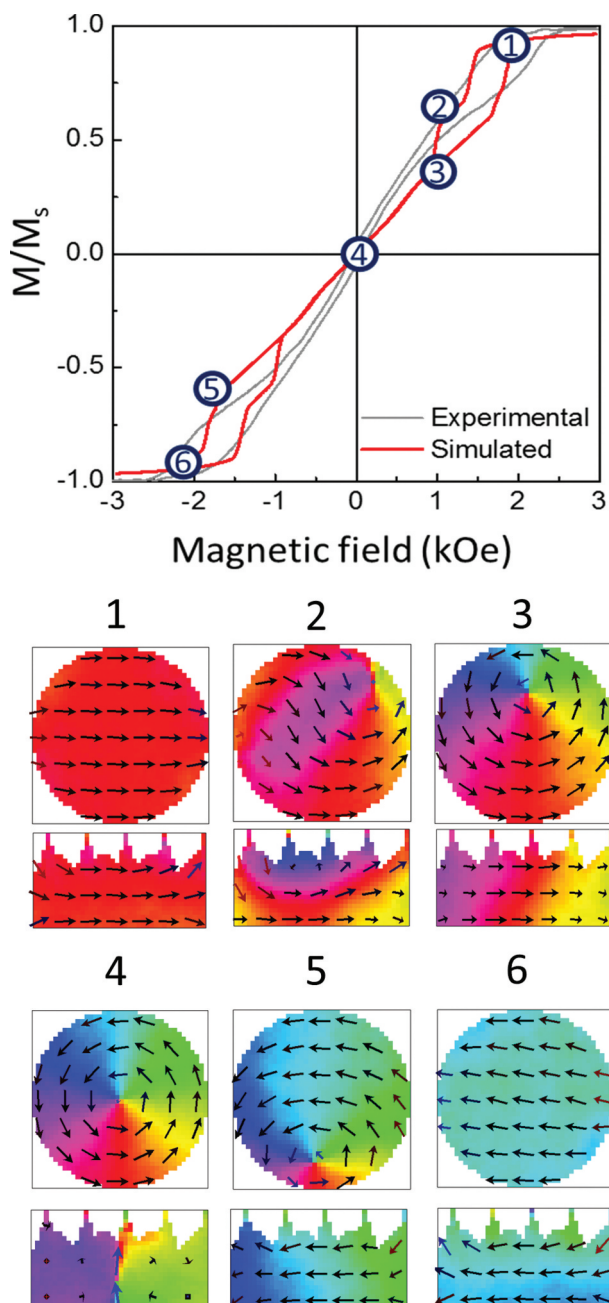


**Figure 3.** Micromagnetic modelling of the magnetic behavior of the as-prepared nanopillars. The hysteresis loop was modelled using an array of four rough Co nanopillars with geometry mimicking the experimentally observed one. Characteristic spin configurations, at different values of applied magnetic field. [(1)–(6)] correspond to the magnetic structure of an individual rough Co nanopillar from the array. For each configuration the horizontal cross-section through the center (at half the height) and the vertical cross-section through the diameter of the pillar are shown in a circle and the rectangle below, respectively. The diameter of the pillars is 200 nm and the thickness is 60 nm with 20 nm added roughness. The black arrows represent the in-plane orientations of the magnetic moments. In the cross-section configurations, the red color is defined by the magnetization pointing to the right side, and the cyan color is for magnetization pointing left.

(b)). In this case, the hysteresis loop becomes squarer and it opens in the central part, resulting in higher coercive field (i.e. tending to single-domain state with

in-plane magnetic anisotropy). Obviously, none of the two simulated loops agree with the experimentally obtained data.

Several magneto-ionic studies indicated that oxygen-ion transport is a complex process and occurs via, at least, two-fold mechanism: (i) homogeneous  $O^{2-}$  migration toward the electrode with the opposite charge (due to Coulombic attraction), and (ii) localized oxygen ion migration along fast diffusion channels [25,48]. Grain boundaries promote the development of sporadic diffusion paths for the oxygen ions, rather than horizontal migration fronts, thus leading to development of multiple  $CoO_x/Co$  interfaces, as it is schematically illustrated in the inset of Figure 4(c). Remarkably, micromagnetic simulations using such pseudo-random arrangement of irregularly shaped Co nanoparticles embedded in the paramagnetic  $CoO_x$  matrix, each of them having its own magnetic easy axis, led to computed hysteresis loops which capture well the experimental one. More specifically, the cluster array was defined by two sets of particles with different periods, shifts and sizes to imitate a kind of random shapes (Figure 5). Due to their small lateral dimensions (10–30 nm), magnetization reversal in each of these Co nanoclusters occurs by coherent rotation, as revealed by the spin configuration modeling at different magnetic fields. Note that some of the Co clusters could easily have even lower sizes and could therefore be superparamagnetic at room temperature.

To shed light on the nanostructural changes that take place under voltage actuation, the composite nanopillars were inspected using STEM and EELS techniques. Cross-section lamellae from the pristine and voltage-treated nanopillars were prepared. Figure 6(a) shows the STEM image of a non-treated bilayered nanopillar, at interface region between Co and  $GdO_x$ . Figure 6(b) shows a similar zoom after treating the pillar at +50 V for 1 hour. To locally quantify the oxygen distribution, EELS mappings near the Co/ $GdO_x$  interface were conducted. The corresponding inspected areas are highlighted with white rectangles on panels (a) and (b). EELS mappings of Co, Gd and O are shown in Supporting Figure S3. Figure 6(c) shows the oxygen EELS mapping obtained from the pristine nanopillar (0 V, on the left) and in the voltage-treated sample (+50 V, on the right). At 0 V (non-treated sample), clear red (oxygen) and black (no oxygen) regions are observed, corresponding to  $GdO_x$  and oxygen-free (metallic) cobalt. In contrast to the as-grown sample, the EELS mapping of a similar region in the voltage-treated sample suggests oxygen redistribution across the whole inspected area. These results confirm the magneto-ionic mechanism in voltage actuated Co/ $GdO_x$  nanopillars, i.e. under the action of electric field the  $O^{2-}$  ions are driven from  $GdO_x$  towards Co, with oxygen content ~20 at.% in the region below the Co/ $GdO_x$  interface.



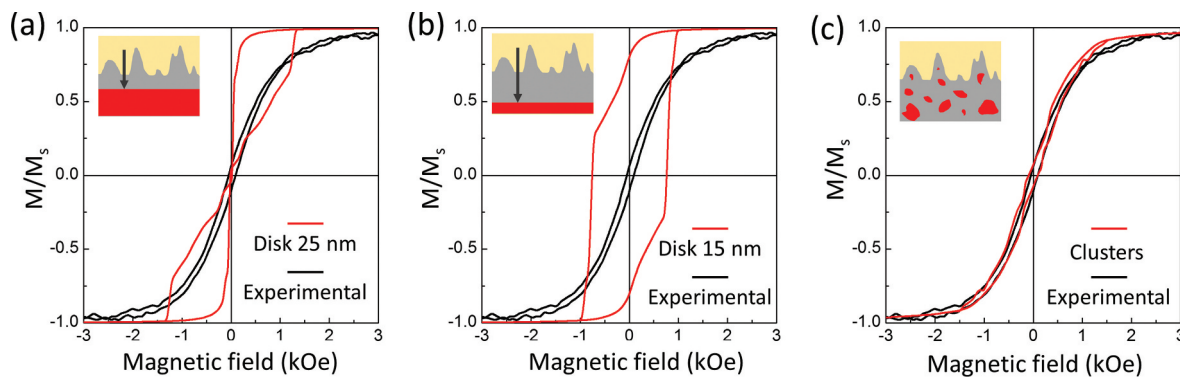


**Figure 4.** Simulated hysteresis loops of an individual Co nanopillar after positive voltage application (e.g.  $\Delta V = 200$  V) considering the formation of (a) a flat Co disk of 25 nm thickness, (b) a flat Co disk of 15 nm thickness, and (c) array of Co clusters with random anisotropy easy axis embedded in a  $\text{CoO}_x$  matrix. The insets of the panels a, b and c show schematic drawings where grey color represents non-magnetic  $\text{CoO}_x$  and red color is for the simulated Co entities.

The Co/ $\text{GdO}_x$  nanopillars treated at +50 V for 1 hour were further investigated by STEM. Figure 7 (a) shows the selected area electron diffraction (SAED) pattern of a region belonging to the Co layer, at about 30 nm from the interface with  $\text{GdO}_x$ . The diffraction pattern corresponding to this area indicates the presence of several phases, including hcp-Co and  $\text{GdO}_x$  (as in the pristine sample, Figure S4(a,b)), and also  $\text{Co}_3\text{O}_4$  as well as metallic Gd, in agreement with the EELS mapping. This implies that indeed oxygen magneto-ionic results in a partial reduction of  $\text{GdO}_x$  and oxidation of metallic Co to an oxide or a mixture of oxides (some of them may be non-stoichiometric especially when larger voltage is applied) [25].

An even smaller region, indicated by the white square in Figure 7(a), was inspected in more detail. Fast Fourier Transform (FFT) analysis of this area shows spots with interplanar distances that correspond to metallic Co and  $\text{Co}_3\text{O}_4$  nanoscale phases (Figure 7(b,c)). Figure 7(d) reveals that this region is actually a zoom of an interface area between the metal and the oxide phases. In order to separate the contributions from each of these two phases, either Co or  $\text{CoO}_x$  reflections were masked via inverse Fourier transform image processing. The area highlighted in red color in Figure 7(e) corresponds to a region with well-distinguishable planes with an average interplanar distance of  $\sim 0.19$  nm, which can be indexed to hcp-Co(101). Likewise, Figure 7(f) shows a region of fcc- $\text{Co}_3\text{O}_4$  (311) with a larger interatomic distance of  $\sim 0.24$  nm, shadowed in yellow color. This data confirms that, for positive applied voltages, oxygen migrates from  $\text{GdO}_x$  and leaves behind irregular metallic Co nano-clusters of different sizes. Note that the size of the individual Co clusters in Figure S4(c) is below 5 nm. In this particular case, such Co nanoclusters would be superparamagnetic, since the critical cluster size that renders superparamagnetic behavior at room temperature for cobalt is below 13 nm [76]. However, the shape of the experimentally obtained

hysteresis loop implies a ferromagnetic behavior with a non-zero coercivity (Figure 2(a)). Hence, most likely, there is a distribution of lateral sizes in the Co clusters, probably being larger towards the substrate, i.e. in regions farther away from the oxygen source. In any case, note that the HR-TEM analysis does not easily allow to evidence the presence of large clusters of either Co or  $\text{CoO}_x$  because at lower magnification the interplanar distances cannot be resolved.

Large voltages of opposite polarity were applied to the sample in order to try to recover the original vortex state. The experimental results demonstrate that, unfortunately, the observed effect appears to be irreversible. No changes in magnetic moment or the shape of the loop could be observed upon voltage gating at  $\Delta V = -200$  V, or even larger negative voltages. Poor reversibility and cyclability are among the main disadvantages of the magneto-ionic mechanism [23]. Generally, the reason for this is the severe voltage-induced phase transformations in pristine materials caused by oxidation/reduction reactions that lead to the development of new phases with distinct structural properties. It has been reported that Co reaction with oxygen proceeds along the forward direction, while the reversible reaction is much less energetically favorable [57]. Furthermore, the propylene carbonate electrolyte used in this work as a dielectric material tends to polymerize at positive voltages (i.e. at the same polarity required to drive the oxygen ions from  $\text{GdO}_x$  towards Co) [77]. Experimentally, it had been observed that polymerization starts already at +14 V [56], but the system investigated here requires much larger positive voltages to switch between the magnetic states. Unfortunately, propylene carbonate cannot be depolymerized with voltage of opposite polarity. Thus, the organic products accumulated at the surface of the magnetic material significantly reduce the effective electric field and therefore hamper magneto-ionic cycling. Another factor that should also be considered is the ionic conductivity of the oxygen source. For

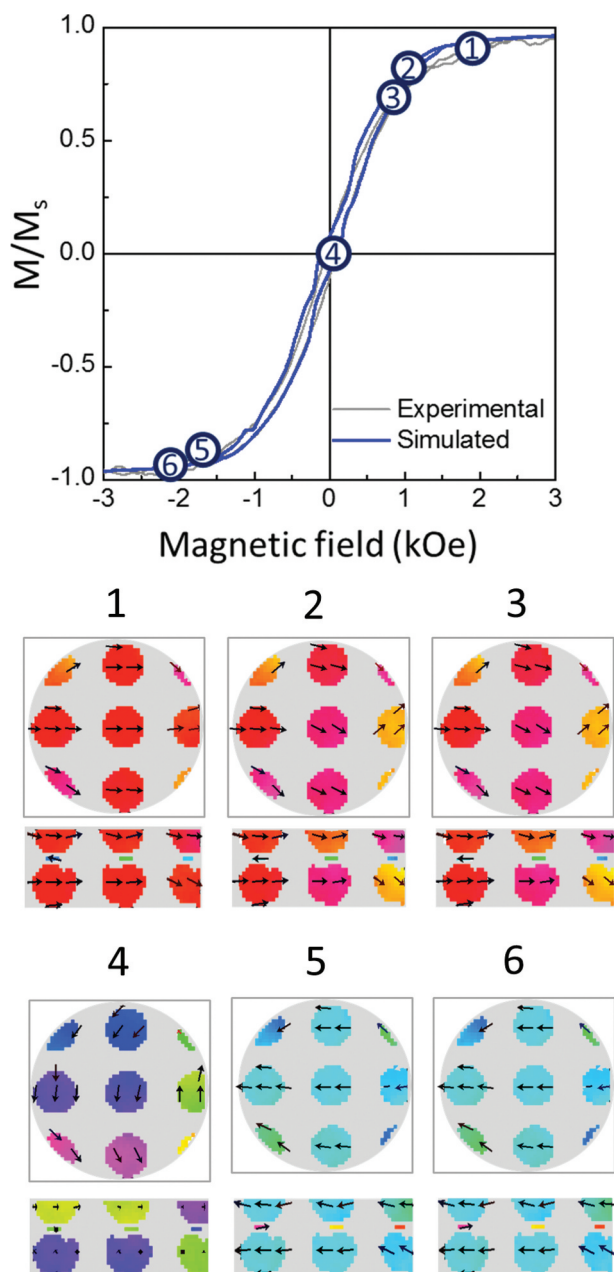


**Figure 5.** Micromagnetic modelling of characteristic spin configurations, at different values of applied magnetic field, of an individual rough Co nanopillar after positive voltage bias. [(1)–(6)] Correspond to the magnetic structure of irregularly shaped Co nanoclusters embedded in paramagnetic  $\text{CoO}_x$  matrix (shown as grey background). The black arrows represent the orientations of the magnetic moments. The horizontal cross-section at the center and the vertical cross-section through the diameter of the pillar are shown as a circle and a rectangle, respectively. The diameter of the disks is 200 nm and those of the clusters in the range of 10–30 nm. The red color is defined by the magnetization pointing to the right side, the cyan color is for magnetization pointing left.

oxygen magneto-ionics, the most commonly utilized solid electrolytes are  $\text{Gd}_2\text{O}_3$  [34,49,57–59],  $\text{HfO}_2$  [61,62], or  $\text{Al}_2\text{O}_3$  [64]. All these materials are characterized by high ionic conductivity. However, it has

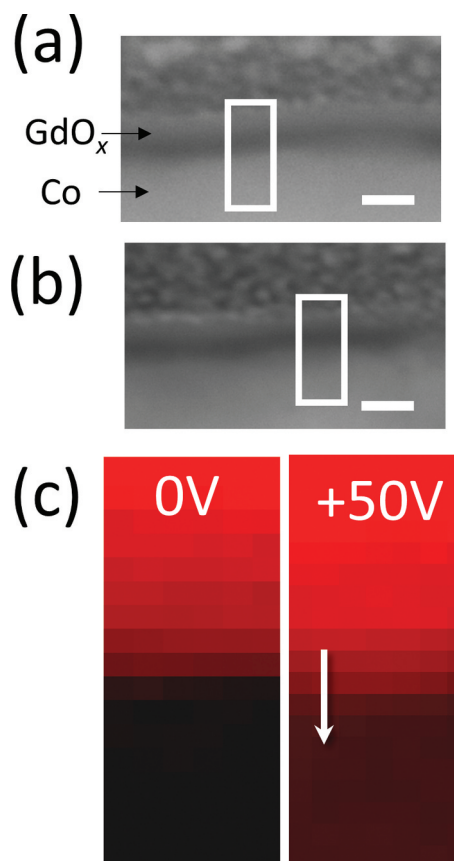


**Figure 6.** Structural and compositional characterization, by HAADF-STEM and EELS, respectively. (a) HAADF of a  $\text{Co}/\text{GdO}_x$  nanopillar prior to voltage actuation, i.e. at 0 V, (b) HAADF of the interface between Co and  $\text{GdO}_x$  after positive voltage bias at  $\Delta V = +50$  V for 1 hour. The scale bar is 40 nm. The white rectangles in panels (a) and (b) correspond to the area inspected by EELS. (c) Characteristic oxygen EELS mappings: left was obtained from (a) and it corresponds to 0 V, whereas (c) right was obtained from panel (b) after applying +50 V. White arrow shows the direction of oxygen ions diffusion towards the substrate.

been reported that, under certain conditions,  $\text{Gd}_2\text{O}_3$  is more prone to transmit oxygen rather than sink it [57]. Under positive voltages,  $\text{AlO}_x$  may exhibit better oxygen donor capabilities but it tends to dissolve/detach for voltages larger than 50 V. In contrast,  $\text{HfO}_2$  is more prone to receive oxygen than to donate it [65], so it does not work as well as  $\text{Gd}_2\text{O}_3$  to induce oxidation of adjacent metals.

Finally, it is also worth mentioning that, although switching between vortex and coherent rotation states in Co nanopillars by voltage-driven oxygen migration is experimentally feasible, the complicated oxygen-ion transport and high voltages required make the system overall difficult to control. However, recent studies on voltage-actuated CoN thin films have demonstrated the occurrence of uniform horizontal ion migration fronts in this system, without occurrence of grain-boundary diffusion channels during voltage bias [48]. In addition, nitrogen magneto-ionics requires lower

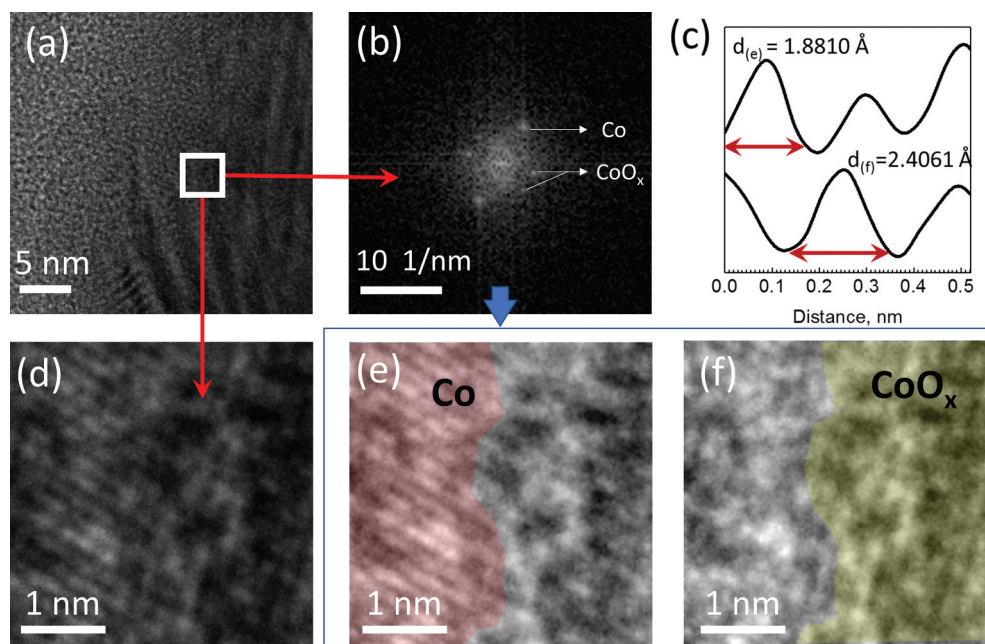


**Figure 7.** Structural characterization by STEM of the sample treated with positive voltage (+50 V for 1 hour): (a) STEM image of an area located at the middle region of the Co pillar; (b) fast Fourier transform of the small region indicated by the white square in the panel (a); (c) average interplanar distances corresponding to the identified hcp-Co(101) and fcc-Co<sub>3</sub>O<sub>4</sub> (311) phases obtained from the panels (e) and (f); (d) magnified STEM image of the sample marked with a white square in the panel (a); (e) hcp-Co planes imaged by masking the contribution from the Co<sub>3</sub>O<sub>4</sub> spots in the FFT; and (f) Co<sub>3</sub>O<sub>4</sub> planes images by masking the hcp-Co reflections.

threshold voltages and has better cyclability than oxygen magneto-ionics. Thus, the way towards reversible control of magnetic vortices will most likely lie beyond oxygen magneto-ionics.

#### 4. Conclusions

Our work demonstrates a new magneto-ionic effect: a proof of concept of voltage-driven magneto-ionic switching from vortex to single-domain magnetization reversal states in heterostructured Co/GdO<sub>x</sub> nanopillars. Large areas can be fabricated at ambient conditions and at low cost by combining electrodeposition with nanoimprint lithography. A positive voltage drives the O<sup>2-</sup> ions from the GdO<sub>x</sub> towards the substrate thus resulting in partial oxidation of metallic Co to paramagnetic CoO<sub>x</sub>. Due to the complicated oxygen-ion transport mechanism, which most likely involves stochastic diffusion channels associated with grain boundaries, oxygen magneto-ionics promotes the formation of irregularly shaped Co clusters randomly distributed within the CoO<sub>x</sub> matrix. Micromagnetic modelling of the system in initial and voltage-actuated states reveals that such clusters behave as single-domain particles whose spins rotate coherently with the applied magnetic field. Under the experimental conditions of this work, the induced switching is irreversible and

requires relatively high voltages. Nevertheless, the concept can be potentially extended to room-temperature nitrogen magneto-ionics (e.g. in CoN) or other magneto-ionic systems with a better cyclability and more controllable ion-migration mechanism, thereby allowing for the development of a unique energy-efficient actuation protocol to control the magnetization reversal mechanism of patterned structures after sample growth, just by applying suitable voltage protocols. From a technological viewpoint, voltage-assisted transitions from vortex to single-domain states are interesting for potential application in stochastic computing (i.e. if the direction of the magnetization in the Co clusters is random), multi-state memories or neuro-morphic computing (where cumulative effects upon successive voltage application are needed), provided the good reversibility and durability of the system.

#### Acknowledgments

This work has received funding from the European Union's Horizon 2020 research and innovation programme under the Marie Skłodowska-Curie grant agreement N° 892661-MAGNUS. Financial support by the European Research Council (MAGIC-SWITCH 2019-Proof of Concept Grant (N° 875018)), the Spanish Ministerio de Ciencia e Innovación through grants, MAT2017-86357-C3-1-R, PID2019-106860GB-I00, PID2020-116844RB-C21 and The Spanish

Severo Ochoa Centre of Excellence program FUNFUTURE (CEX2019-000917-S as well as associated FEDER. The Generalitat de Catalunya (2017-SGR-292 and 2018-LLAV-00032) is also acknowledged. P.M acknowledges financial support from an FPI contract (2017) of the MICINN (Spain) cofounded by the ESF and the UAB.

## Disclosure statement

No potential conflict of interest was reported by the author(s).

## Funding

This work was supported by the Generalitat de Catalunya [2017-SGR-292,2018-LLAV-00032]; European Research Council [875018]; Marie Skłodowska-Curie [892661]; and Spanish Ministry of Science and Innovation [CEX2019-000917-S,MAT2017-86357-C3-1-R,PID2019-106860GB-I00, PID2020-116844RB-C21].

## ORCID

Yu Chen  <http://orcid.org/0000-0003-1651-3698>  
 Aliona Nicolenco  <http://orcid.org/0000-0003-4624-2163>  
 Pau Molet  <http://orcid.org/0000-0003-3693-0309>  
 Agustin Mihi  <http://orcid.org/0000-0003-3821-7881>  
 Eva Pellicer  <http://orcid.org/0000-0002-8901-0998>  
 Jordi Sort  <http://orcid.org/0000-0003-1213-3639>

## Data availability

The raw/processed data required to reproduce these findings cannot be shared at this time as the data also form part of an ongoing study. The data that support the findings of this study are available from the corresponding authors on request.

## References

- [1] Ross CA, Hwang M, Shima M, et al. Micromagnetic behavior of electrodeposited cylinder arrays. *Phys Rev B*. 2020;65:144417.
- [2] Sort J, Buchanan KS, Novosad V, et al. Imprinting vortices into antiferromagnets. *Phys Rev Lett*. 2006;97:67201.
- [3] Ivanov YP, Chuvilin A, Vivas LG, et al. Single crystalline cylindrical nanowires-toward dense 3D arrays of magnetic vortices. *Sci Rep*. 2016;6:23844.
- [4] Yan M, Leaf G, Kaper H, et al. Spin-wave modes in a cobalt square vortex: micromagnetic simulations. *Phys Rev B*. 2006;73:14425.
- [5] Cowburn RP. Change of direction. *Nat Mater*. 2007;6:255–256.
- [6] Dussaux A, Georges B, Grollier J, et al. Large micro-wave generation from current-driven magnetic vortex oscillators in magnetic tunnel junctions. *Nat Commun*. 2010;1:8.
- [7] Jones D, Zou J, Zhang S, et al. Energy storage in magnetic textures driven by vorticity flow. *Phys Rev B*. 2020;102:140411(R).
- [8] Kim DH, Rozhkova EA, Ulasov IV, et al. Biofunctionalized magnetic-vortex microdiscs for targeted cancer-cell destruction. *Nat Mater*. 2010;9:165–171.
- [9] Kim DH, Karavayev P, Rozhkova EA, et al. Mechanoresponsive system based on sub-micron chitosan-functionalized ferromagnetic disks. *J Mater Chem*. 2011;21:8422–8426.
- [10] Wu K, Su D, Liu J, et al. Magnetic nanoparticles in nanomedicine: a review of recent advances. *Nanotechnology*. 2019;30:502003.
- [11] Prejbeanu IL, Natali M, Buda LD, et al. In-plane reversal mechanisms in circular Co dots. *J Appl Phys*. 2002;91:7343–7345.
- [12] Agramunt-Puig S, Del-Valle N, Navau C, et al. Controlling vortex chirality and polarity by geometry in magnetic nanodots. *Appl Phys Lett*. 2014;104:12407.
- [13] Goiriena-Goikoetxea M, Guslienko KY, Rouco M, et al. Magnetization reversal in circular vortex dots of small radius. *Nanoscale*. 2017;9:11269–11278.
- [14] Liu XL, Yang Y, Wu JP, et al. Novel magnetic vortex nanorings/nanodiscs: synthesis and theranostic applications. *Chin Phys B*. 2015;24:127505.
- [15] Sheng Q, Liu XL, Chen WJ, et al. Phase diagrams of magnetic state transformations in multiferroic composites controlled by size, shape and interfacial coupling strain. *AIP Adv*. 2017;7:105221.
- [16] Yamada K, Kasai S, Nakatani Y, et al. Electrical switching of the vortex core in a magnetic disk. *Nat Mater*. 2007;6:270–273.
- [17] Liu Y, Gliga S, Hertel R, et al. Current-induced magnetic vortex core switching in a permalloy nanodisk. *Appl Phys Lett*. 2007;91:112501.
- [18] Fu X, Pollard SD, Chen B, et al. Optical manipulation of magnetic vortex visualized in situ by 4D electron microscopy. *Sci Adv*. 2018;4:eaat3077.
- [19] Le Guyader L, El Moussaoui S, Buzzi M, et al. Demonstration of laser induced magnetization reversal in GdFeCo nanostructures. *Appl Phys Lett*. 2012;101:22410.
- [20] Wang J. Mechanical control of magnetic order: from phase transition to skyrmions. *Ann Rev Mater Res*. 2019;49:361–388.
- [21] Sort J, Hoffmann A, Chung S-H, et al. Magnetization reversal in submicron disks: exchange biased vortices. *Phys Rev Lett*. 2005;95:67201.
- [22] Gilbert DA, Ye L, Varea A, et al. A new reversal mode in exchange coupled antiferromagnetic/ferromagnetic disks: distorted viscous vortex. *Nanoscale*. 2015;7:9878–9885.
- [23] Hu JM, Nan CW. Opportunities and challenges for magnetoelectric devices. *APL Mater*. 2019;7:80905.
- [24] Quintana A, Zhang J, Isarain-Chávez E, et al. Voltage-induced coercivity reduction in nanoporous alloy films: a boost toward energy-efficient magnetic actuation. *Adv Funct Mater*. 2017;27:1701904.
- [25] Quintana A, Menéndez E, Liedke MO, et al. Voltage-controlled ON-OFF ferromagnetism at room temperature in a single metal oxide film. *ACS Nano*. 2018;12:10291.
- [26] Zehner J, Soldatov I, Schneider S, et al. Voltage-controlled deblocking of magnetization reversal in thin films by tunable domain wall interactions and pinning sites. *Adv Electron Mater*. 2020;6:2000406.

- [27] Zehner J, Huhnstock R, Oswald S, et al. Nonvolatile electric control of exchange bias by a redox transformation of the ferromagnetic layer. *Adv Electron Mater.* 2019;5:1900296.
- [28] Shimamura K, Chiba D, Ono S, et al. Electrical control of Curie temperature in cobalt using an ionic liquid film. *Appl Phys Lett.* 2012;100:122402.
- [29] Li X, Lee A, Razavi SA, et al. Voltage-controlled magnetoelectric memory and logic devices. *MRS Bull.* 2018;43:970–977.
- [30] Su W, Wang Z, Chen Y, et al. Reconfigurable magnetoresistive sensor based on magnetoelectric coupling. *Adv Electron Mater.* 2020;6:1901061.
- [31] Molinari A, Hahn H, Kruk R. Voltage-control of magnetism in all-solid-state and solid/liquid magnetoelectric composites. *Adv Mater.* 2019;31:1806662.
- [32] Navarro-Senent C, Quintana A, Menéndez E, et al. Electrolyte-gated magnetoelectric actuation: phenomenology, materials, mechanisms, and prospective applications. *APL Mater.* 2019;7:30701.
- [33] Duschek K, Petr A, Zehner J, et al. All-electrochemical voltage-control of magnetization in metal oxide/metal nanoislands. *J Mater Chem C.* 2018;6:8411–8417.
- [34] Bi C, Liu Y, Newhouse-Illige T, et al. Reversible control of Co magnetism by voltage-induced oxidation. *Phys Rev Lett.* 2014;113:267202.
- [35] Cherifi RO, Ivanovskaya V, Phillips LC, et al. Electric-field control of magnetic order above room temperature. *Nat Mater.* 2014;13:345–351.
- [36] Molinari A, Hahn H, Kruk R. Voltage-controlled on/off switching of ferromagnetism in manganite supercapacitors. *Adv Mater.* 2018;30:1703908.
- [37] Kim HKD, Schelhas LT, Keller S, et al. Magnetoelectric control of superparamagnetism. *Nano Lett.* 2013;13:884–888.
- [38] Gößler M, Albu M, Klinser G, et al. Magneto-ionic switching of superparamagnetism. *Small.* 2019;15:1904523.
- [39] Waser R, Dittmann R, Staikov C, et al. Redox-based resistive switching memories nanoionic mechanisms, prospects, and challenges. *Adv Mater.* 2009;21:2632–2663.
- [40] Pertsev NA, Kohlstedt H. Resistive switching via the converse magnetoelectric effect in ferromagnetic multilayers on ferroelectric substrates. *Nanotechnology.* 2010;21:475202.
- [41] Manchon A, Pizzini S, Vogel J, et al. X-ray analysis of the magnetic influence of oxygen in Pt/Co/AlO<sub>x</sub> trilayers. *J Appl Phys.* 2008;103:07A912.
- [42] Manchon A, Ducruet C, Lombard L, et al. Analysis of oxygen induced anisotropy crossover in Pt/Co/MO<sub>x</sub> trilayers. *J Appl Phys.* 2008;104:43914.
- [43] Ghidini M, Mansell R, Pellicelli R, et al. Voltage-driven annihilation and creation of magnetic vortices in Ni discs. *Nanoscale.* 2020;12:5652–5657.
- [44] Gilbert I, Chavez AC, Pierce DT, et al. Magnetic microscopy and simulation of strain-mediated control of magnetization in PMN-PT/Ni nanostructures. *Appl Phys Lett.* 2016;109:162404.
- [45] Li Q, Tan A, Scholl A, et al. Electrical switching of the magnetic vortex circulation in artificial multiferroic structure of Co/Cu/PMN-PT(011). *Appl Phys Lett.* 2017;110:262405.
- [46] Sun E, Cao W. Relaxor-based ferroelectric single crystals: growth, domain engineering, characterization and applications. *Prog Mater Sci.* 2014;65:124–210.
- [47] Kong S, Kumar N, Checchia S, et al. Defect-driven structural distortions at the surface of relaxor ferroelectrics. *Adv Funct Mater.* 2019;29:1900344.
- [48] De Rojas J, Quintana A, Lopeandía A, et al. Voltage-driven motion of nitrogen ions: a new paradigm for magneto-ionics. *Nat Commun.* 2020;11:5871.
- [49] Tan AJ, Huang M, Avci CO, et al. Magneto-ionic control of magnetism using a solid-state proton pump. *Nat Mater.* 2019;18:35–41.
- [50] Zhang Q, Luo X, Wang L, et al. Lithium-ion battery cycling for magnetism control. *Nano Lett.* 2016;16:583–587.
- [51] Dasgupta S, Das B, Knapp M, et al. Intercalation-driven reversible control of magnetism in bulk ferromagnets. *Adv Mater.* 2014;26:4639–4644.
- [52] Zhou W, Tong WY, Wang Y, et al. Joint theoretical and experimental study on the effects of the salts in the graphite-based dual-ion batteries. *J Phys Chem C.* 2019;123:18132–18141.
- [53] Gößler M, Topolovec S, Krenn H, et al. Nanoporous Pd<sub>1-x</sub>Co<sub>x</sub> for hydrogen-intercalation magneto-ionics. *APL Mater.* 2021;9:41101.
- [54] Vasala S, Jakob A, Wissel K, et al. Reversible tuning of magnetization in a ferromagnetic Ruddlesden-Popper-type manganite by electrochemical fluoride-ion intercalation. *Adv Electron Mater.* 2020;6:1900974.
- [55] Robbenolt S, Menéndez E, Quintana A, et al. Reversible, electric-field induced magneto-ionic control of magnetism in mesoporous cobalt ferrite thin films. *Sci Rep.* 2019;9:10804.
- [56] Navarro-Senent C, Fornell J, Isarain-Chávez E, et al. Large magnetoelectric effects in electrodeposited nanoporous microdisks driven by effective surface charging and magneto-ionics. *ACS Appl Mater Interfaces.* 2018;10:44897–44905.
- [57] Gilbert DA, Grutter AJ, Arenholz E, et al. Structural and magnetic depth profiles of magneto-ionic heterostructures beyond the interface limit. *Nat Commun.* 2016;7:12264.
- [58] Mishra R, Kumar D, Yang H. Oxygen-migration-based spintronic device emulating a biological synapse. *Phys Rev Appl.* 2019;11:54065.
- [59] Sakamaki M, Amemiya K. Observation of an electric field-induced interface redox reaction and magnetic modification in GdO<sub>x</sub>/Co thin film by means of depth-resolved X-ray absorption spectroscopy. *Phys Chem Chem Phys.* 2018;20:20004–20009.
- [60] Bauer U, Yao L, Tan AJ, et al. Magneto-ionic control of interfacial magnetism. *Nat Mater.* 2015;14:174–181.
- [61] Zhou X, Yan Y, Jiang M, et al. Role of oxygen ion migration in the electrical control of magnetism in Pt/Co/Ni/HfO<sub>2</sub> films. *J Phys Chem C.* 2016;120:1633–1639.
- [62] Herrera Diez L, Liu YT, Gilbert DA, et al. Nonvolatile ionic modification of the Dzyaloshinskii-Moriya interaction. *Phys Rev Appl.* 2019;12:34005.
- [63] Robbenolt S, Yu P, Nicolenco A, et al. Magneto-ionic control of magnetism in two-oxide nanocomposite thin films comprising mesoporous cobalt ferrite conformally nanocoated with HfO<sub>2</sub>. *Nanoscale.* 2020;12:5987–5994.
- [64] Van Den Brink A, Van Der Heijden MAJ, Swagten HJM, et al. Large time-dependent coercivity and resistivity modification under sustained voltage application in a Pt/Co/AlO<sub>x</sub>/Pt junction. *J Appl Phys.* 2015;117:17C717.

- [65] Navarro-Senent C, Quintana A, Isarain-Chávez E, et al. Enhancing magneto-ionic effects in magnetic nanostructured films via conformal deposition of nanolayers with oxygen acceptor/donor capabilities. *ACS Appl Mater Interfaces*. 2020;12:14484–14495.
- [66] Matricardi C, Garcia-Pomar JL, Molet P, et al. High-throughput nanofabrication of metasurfaces with polarization-dependent response. *Adv Opt Mater*. 2020;82:000786.
- [67] Gibert-Roca M, Molet P, Mihi A, et al. Near infrared organic photodetectors based on enhanced charge transfer state absorption by photonic architectures. *J Mater Chem C*. 2020;8:9688–9696.
- [68] Molet P, Gil-Herrera LK, Garcia-Pomar JL, et al. Large area metasurfaces made with spherical silicon resonators. *Nanophotonics*. 2020;9:943–951.
- [69] Vernickaite E, Tsyntaru N, Cesiulis H. Electrodeposition and corrosion behaviour of nanostructured cobalt–tungsten alloys coatings. *Trans Inst Met Finish*. 2016;94:313–321.
- [70] Schneider CA, Rasband WS, Eliceiri KW. NIH image to ImageJ: 25 years of image analysis. *Nat Methods*. 2012;9:671–675.
- [71] Robbenolt S, Nicolenco A, Mercier Fernandez P, et al. Electric field control of magnetism in iron oxide nanoporous thin films. *ACS Appl Mater Interfaces*. 2019;11:37338–37346.
- [72] De Rojas J, Quintana A, Lopeandía A, et al. Boosting room-temperature magneto-ionics in a non-magnetic oxide semiconductor. *Adv Funct Mater*. 2020;30:2003704.
- [73] Donahue MJ, Porter G. OOMMF user's guide, version 1.0 OOMMF user's guide, version 1.0. 1999.
- [74] Haratani S, Aoyama T, Sato I. Micromagnetic simulations of polycrystalline cobalt islands for patterned media. *IEEE Trans Magn*. 2000;36:3164–3166.
- [75] Arscott S. SU-8 as a material for lab-on-a-chip-based mass spectrometry. *Lab Chip*. 2014;14:3668.
- [76] Qiao R, Zhang XL, Qiu R, et al. Fabrication of superparamagnetic cobalt nanoparticles-embedded block copolymer microcapsules. *J Phys Chem C*. 2007;111:2426–2429.
- [77] Xiao S, Kolb JF, Malik MA, et al. Electrical breakdown and dielectric recovery of propylene carbonate. *IEEE Trans Plasma Sci*. 2006;34:1653–1661.